Journal of Materials Research and Technology 42 (2026) 7894–7906

Contents lists available at ScienceDirect

Journal of Materials Research and Technology

journal homepage: www.elsevier.com/locate/jmrt

Novel Fe–Ni–Si alloys with a balanced property set for electrical machines

Wei Hock Teh [a,1], Li Ping Tan [b,1], Shilin Chen [a], Coryl Jing Jun Lee [a], Fengxia Wei [a,e], Yakai Zhao [a,d], Shakti P. Padhy [b,f], V. Chaudhary [c,*], Cheng Cheh Tan [a,d,**], R.V. Ramanujan [b,***]

[a] Institute of Materials Research and Engineering (IMRE), Agency for Science, Technology and Research (A*STAR), 2 Fusionopolis Way, Innovis #08-03, 138634, Singapore
[b] School of Materials Science and Engineering, Nanyang Technological University, 639798, Singapore
[c] Department of Mechanical Engineering, Chalmers University of Technology, SE-41296, Gothenburg, Sweden
[d] Future Energy Acceleration & Translation (FEAT), Agency for Science, Technology and Research (A*STAR), 2 Fusionopolis Way, Innovis #08-03, 138634, Singapore
[e] Mark Wainwright Analytical Centre, University of New South Wales, Sydney, NSW, 2052, Australia
[f] J. Mike Walker '66 Department of Mechanical Engineering, Texas A&M University, College Station, TX, 77843, United States

ARTICLE INFO

Keywords:
Magnetic alloys
Fe–Ni–Si system
Multiple properties
Structure-property relations

ABSTRACT

Alloys that simultaneously exhibit good magnetic properties, high mechanical strength, and elevated electrical resistivity are critical for next-generation high-speed, high-torque electrical machines used in electric mobility and energy systems. The development of such novel alloys requires a balanced property set. However, binary Fe–Si and Fe–Ni alloys do not possess the desired combination of mechanical, magnetic and electrical properties. In earlier work, promising regions and compositions in the ternary Fe–Ni–Si system were identified via high throughput screening. Based on the results, we studied in this work a promising high-Ni–Si region (35–40 wt% Ni, 6–10 wt% Si) and a relatively low-solute composition, Fe–11.5Ni–2.7Si, using directed energy deposition and arc melting, to decouple compositional and processing effects. High-Ni–Si alloys exhibited extensive intergranular intermetallic network formation, resulting in high hardness but severe embrittlement. In contrast, Fe–11.5Ni–2.7Si stabilized as a single-phase BCC matrix and exhibited an attractive combination of properties: yield strength of 551 MPa, ultimate tensile strength of 709 MPa, elongation of 4.8%, resistivity of 105 μΩ cm, saturation magnetization of 199 emu/g and coercivity of 14 Oe. These results identify Fe–11.5Ni–2.7Si as a novel Fe–Ni–Si alloy composition that balances mechanical, electrical, and magnetic performance. These results demonstrate that intermetallic phase fraction and connectivity govern the trade-off between mechanical, magnetic, and electrical properties. Controlling phase architecture through composition and processing provides a viable design strategy for multifunctional magnetic structural alloys.

1. Introduction

The electrification of transportation, energy, and power systems has resulted in a growing demand for magnetic alloys that also exhibit high mechanical strength and elevated electrical resistivity [1]. In applications such as high-speed, high-torque electric motors for electric mobility, magnetic materials must withstand large centrifugal stresses while minimizing electrical losses [2–4]. However, no existing alloy composition meets these three requirements simultaneously.

Conventional magnetic alloys illustrate these trade-offs. Binary Fe–Ni and ternary Fe–Ni–Co alloys exhibit high saturation magnetization and low coercivity, together with moderate strength; however, they suffer from low resistivity. In the ternary case, there is a dependence on cobalt, an expensive and supply-critical element [5–11]. In contrast, high Si content Fe–Si alloys possess higher resistivity, lowering eddy current losses, but become brittle at elevated Si content due to the

* Corresponding author.
** Corresponding author. Institute of Materials Research and Engineering (IMRE), Agency for Science, Technology and Research (A*STAR), 2 Fusionopolis Way, Innovis #08-03, 138634, Singapore.
*** Corresponding author.
E-mail addresses: varunc@chalmers.se (V. Chaudhary), dennis_tancc@a-star.edu.sg (C.C. Tan), ramanujan@ntu.edu.sg (R.V. Ramanujan).
[1] Authors contributed equally.

https://doi.org/10.1016/j.jmrt.2026.05.044
Received 22 February 2026; Received in revised form 18 April 2026; Accepted 5 May 2026
Available online 6 May 2026

presence of the ordered B2 and $D0_3$ phases [12–16]. Pure Fe, Ni, and Co similarly fail to achieve a balanced property set, with each sacrificing at least one critical property.

These trends are summarized in Table 1, which compiles hardness, electrical resistivity, saturation magnetization, and coercivity values from our previous studies on compositionally graded alloys processed by directed energy deposition (DED) under similar conditions [17–19], and highlights the trade-offs between the properties. It was hypothesized that a combination of Fe, Ni and Si in a ternary Fe–Ni–Si system could possess a balanced property set. Hence ternary Fe–Ni–Si alloys were studied for a better combination of magnetic, mechanical and electrical properties.

To overcome the intrinsic limitations of conventional alloy systems, alternative strategies have been explored, including amorphous and nanocrystalline alloys [20–24], high-entropy and multi-component systems [25–27], and complex phase architectures [28–30]. Amorphous and nanocrystalline alloys are attractive, especially in applications where efficiency and size reductions are critical, due to advantages like low core losses, high saturation flux and excellent permeability [31]. However, their widespread use is often limited by constraints in bulk manufacturability, restricted component geometries, and processing complexity associated with rapid solidification or controlled nanocrystallization routes, leading to lower commercial adoption [32]. High entropy and multi-component systems, and complex phase architectures often entail challenges related to scalability and processing complexity. In contrast, identification of bulk crystalline alloys capable of providing a combination of mechanical capability and magnetic properties remain underexplored. Thus, the focus of this work is on bulk crystalline alloys for multifunctional performance.

Additive manufacturing (AM), specifically the DED process, offers an attractive alternative. Rapid solidification enables the formation of non-equilibrium phases [33–39], steep thermal gradients promote texture control [40,41], and compositional flexibility facilitates high-throughput exploration of composition–property relationships [42]. DED had been shown to suppress brittle intermetallic formation in Fe–Si alloys at Si content levels of up to 20 wt% [18]; DED was able to generate compositionally graded libraries that map composition, phase constitution, and material properties in the Fe–Si [18], Fe–Ni–Co [17], and Fe–Ni–Si [19] systems.

Our recent high-throughput DED investigation of Fe–Ni–Si alloys revealed two notable findings [19]:

(i) a high-Ni–Si regime (35–40 wt% Ni, 6–10 wt% Si) exhibiting hardness values exceeding 600 HV, unprecedented for Fe-based soft magnetic alloys; and
(ii) a low-solute composition, Fe–11.5Ni–2.7Si, displaying a promising balance of hardness, resistivity, and magnetic softness.

However, these results were derived from compositionally graded builds, in which grain size and microstructure varied continuously, and therefore did not allow direct validation of bulk properties or detailed mechanistic understanding.

Hence, the present work focuses on three compositions of greatest interest (Fe–36Ni–10Si, Fe–45Ni–10Si, and Fe–11.5Ni–2.7Si), fabricated by both DED and arc melting to establish robust processing–structure–property relationships. This approach enables decoupling of the compositional effects from microstructural gradients and provides insight into the role of solidification conditions on the phase evolution and the property response. We identified the mechanisms responsible for exceptionally high hardness observed in high-Ni–Si alloys and validated the multi-property performance of Fe–11.5Ni–2.7Si in bulk form.

Our results demonstrate that the intermetallic phase content is a governing factor in tailoring the mechanical, magnetic, and electrical properties in Fe–Ni–Si alloys. Increasing the ordered phase content enhances the hardness and electrical resistivity but reduces the ductility and magnetic properties. Conversely, stabilization of a single-phase matrix enables a more balanced property profile. This insight provides a mechanistic framework for property optimization and identifies the ternary Fe–11.5Ni–2.7Si composition as a promising candidate for applications requiring the desired property set.

2. Experimental procedures

2.1. Powder feedstock and alloy fabrication

High-purity gas-atomized elemental powders of Fe (99.95%), Ni (99.95%), and Si (99.9%) were procured from Sandvik Osprey Ltd. (UK) and Tosoh SMD Inc. (USA). Powders with particle sizes of 63–150 μm were used to prepare Fe–11.5Ni–2.7Si, Fe–36Ni–10Si, and Fe–45Ni–10Si (all in wt.%).

Alloys were fabricated by both DED and arc melting to enable comparison of additively manufactured and bulk-processed materials. DED builds were produced using an Optomec LENS 150 system under an argon atmosphere, employing processing parameters optimized in our prior studies, to achieve near-full density with minimal cracking [17–19]. The parameters were: laser power 350 W, layer thickness 0.20 mm, hatch spacing 0.20 mm, and laser speed 8.46 mm/s. Arc melting was conducted in a MRF ABJ-900 furnace under high-purity argon. Powder blends were melted on a water-cooled copper hearth using a tungsten electrode, and each ingot was inverted and re-melted at least five times to ensure chemical homogeneity.

Table 1
Composition-dependent hardness, electrical resistivity, saturation magnetization, and coercivity of DED fabricated elemental and compositionally graded soft magnetic alloys.

Material System	Fe (wt%)	Ni (wt%)	Si (wt%)	Co (wt%)	Hardness ($HV_{1/15}$)	Electrical Resistivity (μΩ cm)	Saturation Magnetization (emu/g)	Coercivity (Oe)	Ref.
Fe	100	-	-	-	143	41.6	219.1	20.8	[17]
Ni	-	100	-	-	89	9.4	61.6	18.7	[17]
Co	-	-	-	100	169	13.3	156.5	66.4	[17]
Fe–Ni	73	27	-	-	117	55.9	186.6	6.5	[17]
	48	52	-	-	116	31.8	146.4	1.5	[17]
	20	80	-	-	119	31.0	102.1	0.5	[17]
Fe–Ni–Co	57	19	-	24	372	31.6	206.1	12.4	[17]
	23	51	-	25	115	25.7	126.8	18.8	[17]
	20	19	-	61	112	25.9	161.7	11.7	[17]
Fe–Si	96	-	4	-	225	70.4	201.9	10.6	[18]
	92	-	8	-	412	115.5	172.1	9.2	[18]
	83	-	17	-	608	117.2	98.1	10.0	[18]
Fe–Ni–Si	72	24	4	-	156	146.2	121.5	42.8	[19]
	48	41	12	-	605	184.4	79.7	13.2	[19]

2.2. Sample preparation, characterization and property measurements

DED-fabricated pillars and arc melted ingots were sectioned using electrical discharge machining (EDM). Cross-sections parallel to the build direction were mounted, ground sequentially using silicon carbide papers (grit sizes 500–4000) and polished to a mirror finish with 0.03 μm colloidal silica suspension.

Porosity and structural integrity were examined using optical microscopy (Olympus BX53 M). Phase identification was performed using X-ray diffraction (XRD) on a Bruker D8 Advance diffractometer, with CuK_α radiation ($\lambda = 1.5406$ Å), operated at 40 kV and 40 mA over a 2θ range of 10–120°. Lattice parameters and phase fractions were determined by Rietveld analysis using TOPAS V5. Grain morphology and crystallographic orientation were analysed by electron backscatter diffraction (EBSD) on a JEOL FESEM IT500HR equipped with an Oxford Symmetry detector, using a step size of 1.5 μm. Elemental distributions and chemical segregation were assessed by energy-dispersive X-ray spectroscopy (EDX) in the same system.

Vickers microhardness was measured using an InnovaTest Falcon 5000 tester with a 1 kgf load and 15 s dwell time. Nanoindentation mapping was performed using a KLA-Tencor G200 nanoindenter with a Berkovich tip to probe intergranular and intragranular regions identified by EBSD and EDX. Tensile testing was performed at room temperature on a MTS Landmark servohydraulic system. Rectangular specimens (46 × 10 mm overall dimensions, gauge section 6 × 2 mm, thickness 1.5 mm, transition radius 2 mm) were machined with the loading axis parallel to the build direction to determine yield strength, ultimate tensile strength, and elongation to failure.

Magnetic properties were measured using a Lakeshore 7400 vibrating sample magnetometer (VSM). Samples of similar size were extracted from representative regions, and hysteresis loops were used to obtain the saturation magnetization (M_s) and coercivity (H_c) values. Electrical resistivity was measured at room temperature using a standard four-point probe (Keithlink), and the results were correlated with local composition obtained from EDX.

3. Results and discussions

The Fe–Ni–Si alloys investigated in this work cover two distinct property regimes: High-Ni, high-Si alloys (Fe–36Ni–10Si and Fe–45Ni–10Si), which exhibited high Vickers hardness values, and the lower solute Fe–11.5Ni–2.7Si alloy, which showed a more balanced combination of mechanical strength, ductility, magnetic properties, and electrical resistivity.

To establish the rationale of the composition selection for the high hardness regime, the high-Ni, high-Si compositionally graded Fe–Ni–Si DED build reported in our prior work was first analysed [19]. Subsequently, selected single (fixed) composition alloys fabricated by both DED and arc melting were examined to decouple grain size effects from the effects of composition. The results are presented in the following sequence:

(i) hardness and segregation trends in selected regions of compositionally graded DED samples,
(ii) processing, composition and phase evolution in DED and arc melted single-composition alloys,
(iii) corresponding microstructural features, phase distribution and local mechanical response,
(iv) bulk properties of single composition alloys, and
(v) structure–property correlations for the single composition alloys.

3.1. Hardness and segregation trends in selected regions of compositionally graded DED sample

Compositionally graded Fe–Ni–Si pillars fabricated by DED enabled rapid screening of property evolution across a broad compositional window (0–40 wt% Ni, 0–10 wt% Si) [19]. Within the high-Ni, high-Si region (35–40 wt% Ni, 6–10 wt% Si), the build remained dense and crack-free despite the elevated Si content (Fig. 1a and b). Vickers hardness measurements revealed a systematic increase in hardness along the build direction, from ~170 HV near the substrate to values exceeding 600 HV in the upper regions (Fig. 1c). Such hardness levels are unusually high for Fe-based magnetic alloys and warranted further microstructural and compositional investigation.

Microstructural analysis using EBSD revealed a clear evolution in morphology along the build height. Near the substrate, the microstructure consisted predominantly of coarse grains aligned with the thermal gradient, whereas regions further from the substrate exhibited finer, more equiaxed grains together with the emergence of continuous intergranular features (Fig. 1c). While these observations suggest a refinement in microstructural scale, it is noted that quantitative grain size analysis was not performed; therefore, the term “refinement” is used here to describe qualitative morphological evolution. This qualitative morphological evolution coincided with higher hardness.

At regions corresponding to the highest hardness (area 3), EDX mapping revealed pronounced segregation of Ni and Si along grain boundaries (Fig. 1d). These segregated regions form interconnected networks that coincide spatially with hardness maxima. Complementary XRD analysis of the whole pillar further identified the emergence of ordered cubic and trigonal phases ($P2_13$, $P321$), consistent with Ni–Si intermetallic compounds (Fig. 1e). Together, these results indicate a combined contribution from grain refinement, intergranular segregation and intermetallic phase formation to the exceptional hardening observed in the high-Ni–Si regime of the Fe–Ni–Si alloys.

The observed behaviour can be rationalized based on thermodynamic and kinetic considerations of the constituent binary systems. As shown in Fig. 2a, the Ni–Si pair exhibits a strongly negative enthalpy of mixing (−80 to −100 kJ/mol) [43], which is significantly more negative than that of Fe–Si (−40 to −60 kJ/mol) [15] and Fe–Ni (~−5 kJ/mol) [44]. This large negative enthalpy reflects the strong chemical affinity between Ni and Si, promoting clustering and a high thermodynamic propensity for compound formation. Under the rapid solidification conditions associated with DED, this thermodynamic driving force is coupled with limited diffusion, resulting in segregation of Ni and Si to grain boundaries and the formation of ordered intermetallic phases (schematically illustrated in Fig. 2b).

These intergranular intermetallic networks serve as effective barriers to dislocation motion, leading to significant strengthening. At the same time, their interconnected morphology partitions the microstructure and promotes strain localization, which has important implications for the mechanical response of the alloy at higher solute content. The exceptionally high hardness observed in the high-Ni–Si regime is therefore attributed to the combined effects of segregation-driven phase formation and the resulting intergranular network architecture, rather than grain size effects alone.

3.2. Single-composition Fe–Ni–Si alloys prepared by DED and arc melting

To validate the high-hardness regime identified in the compositionally graded builds and to decouple the compositional effects from the microstructural gradients, bulk single-composition alloys (Fe–36Ni–10Si, Fe–45Ni–10Si, and Fe–11.5Ni–2.7Si) were fabricated by DED. These larger-volume samples enable the direct assessment of bulk processability and intrinsic structure–property relationships in as-fabricated condition.

The selection of these compositions was guided by the compositional regimes identified in the graded DED study. Fe–36Ni–10Si corresponds to the average composition of the peak hardness region, while Fe–45Ni–10Si was selected to evaluate the effect of further increase of the Ni content on phase stability and mechanical response. The lower solute Fe–11.5Ni–2.7Si composition was previously identified as a

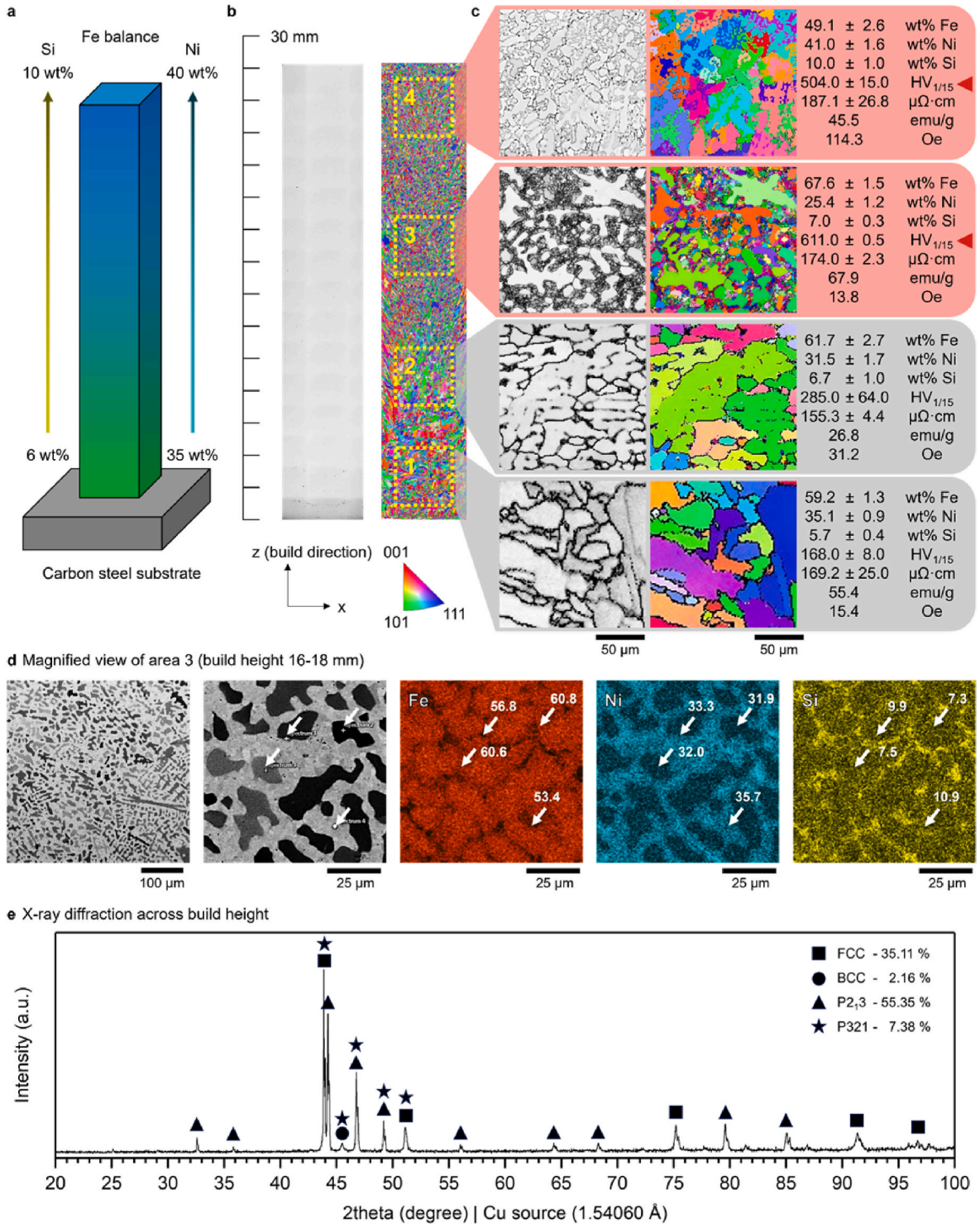

Fig. 1. Evaluation of compositionally graded DED-fabricated Fe–Ni–Si pillars (35–40 wt% Ni, 6–10 wt% Si). (a) Schematic illustrating the programmed composition gradient along the build direction. (b) Optical micrograph showing dense, crack-free deposits despite high Si content. (c) Microstructural evolution and hardness increase (in the range of ~500 – ~600 HV) with increasing distance from the substrate. (d) EDX maps showing preferential Ni–Si segregation along grain boundaries. (e) XRD patterns revealing formation of ordered Ni–Si intermetallic phases, correlating segregation with high hardness.

candidate exhibiting a balanced combination of mechanical strength, magnetic softness, and electrical properties [19]. Studying these fixed compositions enables isolation of the compositional effects from the continuous microstructural variation inherent in graded samples.

DED-fabricated Fe–36Ni–10Si and Fe–45Ni–10Si exhibited extensive cracking throughout the build volume (Fig. 3a). This behaviour is attributed to the formation of interconnected intergranular intermetallic phases in the high-Ni–Si regime as established in Section 3.1. These brittle phase networks significantly reduced the ability of the material to accommodate thermal stresses generated during rapid solidification, leading to crack initiation and propagation across the build.

In contrast, no macroscopic cracking was observed in DED-fabricated Fe–11.5Ni–2.7Si. However, despite its single-phase BCC matrix, the alloy exhibited brittle fracture during handling and could not be

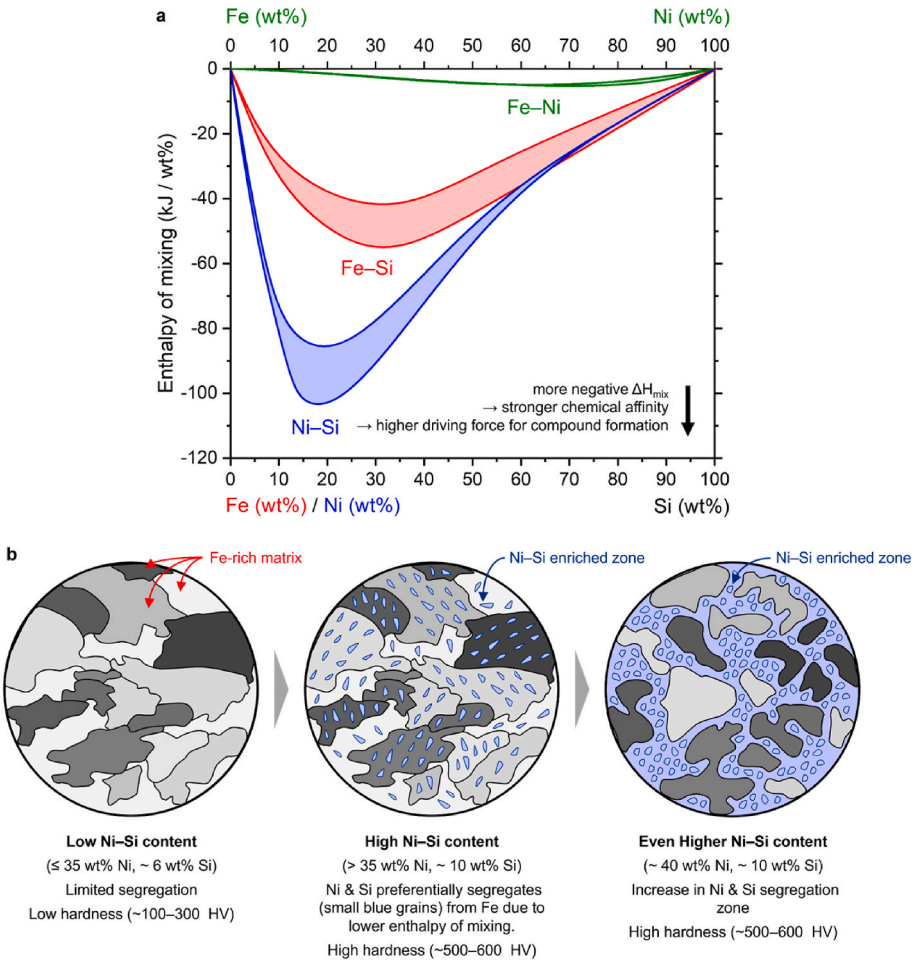

Fig. 2. Thermodynamic basis for Ni–Si segregation and strengthening in Fe–Ni–Si alloys. (a) Enthalpies of mixing (ΔH_{mix}) show that the Ni–Si pair exhibit more negative ΔH_{mix} than Fe–Si or Fe–Ni pairs, indicating the strongest chemical affinity and highest driving force for compound formation [15,43,44]. (b) Schematic illustration of the resulting microstructural evolution: at low solute contents, the microstructure remains largely homogeneous; with increasing Ni and Si, preferential Ni–Si segregation occurs, forming ordered Ni–Si intermetallic clusters (e.g., $P2_13$ and $P321$), which impede deformation and lead to a pronounced increase in hardness.

machined into tensile specimens. This behaviour suggests that, although intergranular intermetallic networks were suppressed at lower solute contents, the combination of fine microstructure and residual thermal stresses inherent to DED processing still led to limited plastic deformation in small-scale builds [45,46].

To further investigate the intrinsic behaviour of these alloys under reduced thermal gradients and near-equilibrium solidification conditions, the same compositions were fabricated by arc melting (Fig. 3b). ***Interestingly, unlike the DED counterparts, the arc melted samples were fully dense and free of visible cracks.*** The larger melt volumes and slower cooling rates promoted compositional homogenization and reduced the driving force for intergranular phase networks, thereby suppressing the macroscopic cracking observed in the rapidly solidified DED samples. This comparison highlights the strong sensitivity of Fe–Ni–Si alloys to the processing route, where the interplay between solidification kinetics, phase formation, and thermal stress governs both microstructural evolution and mechanical integrity.

3.3. Composition and phase evolution: DED versus arc melting

EDX analysis revealed compositional deviations in the DED-fabricated samples relative to their nominal values, most notably in the Si content (Table 2). For example, the measured composition of Fe–45Ni–10Si (nominal) was 44.45 wt% Ni and 12.08 wt% Si, for Fe–36Ni–10Si the measured composition was 34.94 wt% Ni and 9.02 wt % Si, and for Fe–11.5Ni–2.7Si, it was 11.33 wt% Ni and 3.09 wt% Si. These deviations, reaching up to ~2 wt%, were attributed to variations in the powder flowability during deposition. In particular, the irregular morphology of Si powders compared to the more spherical Fe and Ni powders can cause transient fluctuations in the local feed composition under high-Si processing conditions [18].

In contrast, the arc melted samples showed compositions within ±0.5 wt% of their nominal values, reflecting improved chemical homogenization during bulk melting and repeated re-melting cycles. For instance, the measured composition of arc melted Fe–45Ni–10Si (nominal) was 45.49 wt% Ni and 9.86 wt% Si, while that of Fe–36Ni–10Si was 35.73 wt% Ni and 9.87 wt% Si, and that of Fe–11.5Ni–2.7Si was 11.35 wt% Ni and 2.6 wt% Si. These results confirm that compositional variations are inherent to powder-fed additive manufacturing processes but remain within a controlled and quantifiable range.

XRD analysis (Fig. 4) showed pronounced differences in the phase constitution observed for the two processing routes, particularly for high-Ni–Si alloys. DED-processed Fe–36Ni–10Si and Fe–45Ni–10Si alloys exhibited multiphase structures, comprising of disordered BCC and FCC phases together with several ordered intermetallic phases ($P2_13$, $P321$, F-43m). In contrast, the arc melted counterparts were dominated by the FCC phase, with substantially lower phase fractions of intermetallic phases. It is noted that partial peak overlap between the F-43m and the BCC phases introduces some uncertainty in their individual quantification; however, the overall trend of higher ordered phase content in

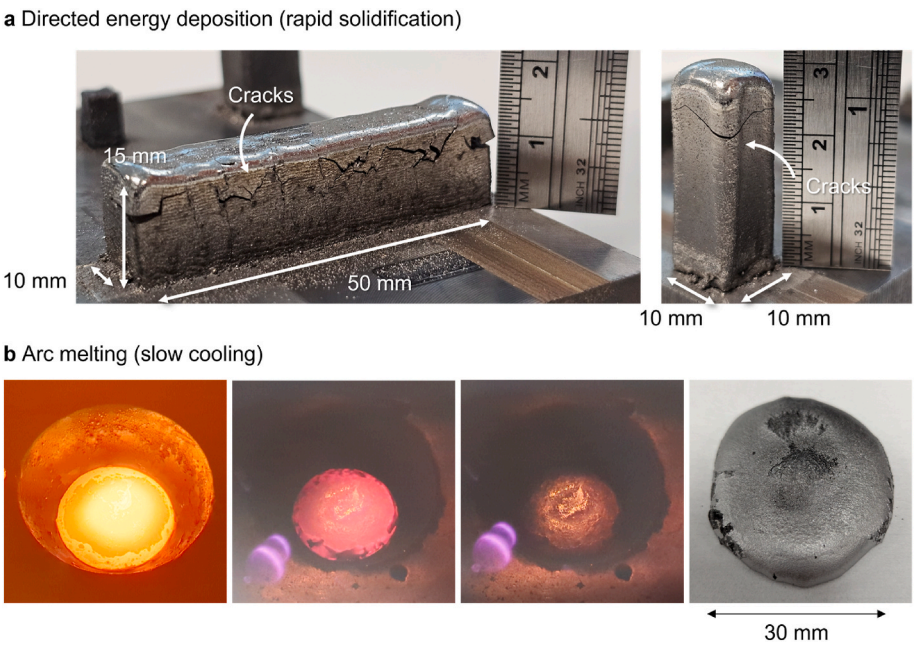

Fig. 3. Macroscopic cracking in high-Ni–Si Fe–Ni–Si alloys processed by DED and arc melting techniques. (a) DED-processed Fe–36Ni–10Si and Fe–45Ni–10Si exhibit severe cracking due to intergranular intermetallics. (b) Arc melted counterparts solidify without visible cracks, showing improved homogeneity under slower cooling.

Table 2
Measured composition (EDX) and phase fractions (Rietveld analysis) of Fe–Ni–Si alloys fabricated by DED and arc melting.

Process	Nominal composition	EDX Fe (wt %)	EDX Ni (wt %)	EDX Si (wt %)	FCC (Disordered) (%)	BCC (Disordered) (%)	$P2_13$ (Ordered cubic) (%)	$P321$ (Ordered trigonal) (%)	F-43m (Ordered cubic) (%)	D03 (Ordered FCC) (%)	B2 (Ordered Cubic) (%)	Sum of ordered phase (%)
DED	Fe–45Ni–10Si	43.47	44.45	12.08	35.77	9.68	10.21	29.63	14.71	-	-	55.55
DED	Fe–36Ni–10Si	56.04	34.94	9.02	25.51	42.22	13.92	7.52	10.83	-	-	32.27
DED	Fe–11.5Ni–2.7Si	85.58	11.33	3.09	-	100	-	-	-	-	-	-
Arc Melt	Fe–45Ni–10Si	44.65	45.49	9.86	65.39	8.03	12.44	7.72	6.42	-	-	26.58
Arc Melt	Fe–36Ni–10Si	54.4	35.73	9.87	58.63	18.58	10.96	2.07	9.76	-	-	22.79
Arc Melt	Fe–11.5Ni–2.7Si	86.05	11.35	2.6	-	100	-	-	-	-	-	-

DED samples is clear.

Rietveld analysis (Table 2) quantified these differences. For Fe–36Ni–10Si, the intermetallic phase fraction was ~32 % in the DED sample compared with ~23 % in the arc melted alloy. An even larger disparity was observed for Fe–45Ni–10Si, where the DED sample contained ~56 % intermetallic phases, compared with ~27 % in the arc melted counterpart. In contrast, Fe–11.5Ni–2.7Si remained single-phase BCC regardless of processing route, consistent with its lower solute content and reduced thermodynamic driving force for ordering.

These microstructural differences directly reflect the distinct thermal histories of the two fabrication processes. DED imposed extremely high cooling rates (~10^2–10^3 K/s [47,48]) and localized compositional fluctuations arising from discrete powder feeding, which promoted solute trapping, supersaturation, and heterogeneous nucleation of ordered Ni–Si intermetallic phases. The strong chemical affinity between Ni and Si further enhanced this tendency, leading to the formation of interconnected intergranular phase networks. In contrast, arc melting is characterized by slower cooling rates (less than 20 K/s [49–51]) and larger melt volumes, enabling enhanced diffusion and chemical homogenization. This reduced segregation and suppressed the formation of ordered intermetallic networks, stabilizing the predominantly disordered FCC or BCC matrices. This processing-dependent phase evolution provides a mechanistic basis for the observed differences in mechanical behaviour. The higher intermetallic phase fractions in DED-fabricated high-Ni–Si alloys contributed to increased hardness but also promoted brittleness and cracking, as discussed in Sections 3.1 and 3.2. Conversely, reduced intermetallic content in arc melted samples enabled improved structural integrity and ductility. These findings highlight the critical role of solidification kinetics in controlling phase constitution and, consequently, multifunctional properties in Fe–Ni–Si alloys.

3.4. Microstructure, phase distribution and local mechanical response

Optical micrographs of cross-sectional samples (Fig. 5a) confirmed extensive cracking in DED-fabricated Fe–36Ni–10Si and Fe–45Ni–10Si alloys, whereas the corresponding arc melted samples and the lower-solute Fe–11.5Ni–2.7Si alloy remained crack-free. These observations are consistent with the processing-dependent phase evolution discussed in Sections 3.2 and 3.3.

Backscattered electron imaging (Fig. 5b) revealed clear differences in microstructural scale and phase contrast between compositions and processing routes. Fe–11.5Ni–2.7Si exhibited relatively larger and more homogeneous grains compared to the high-Ni–Si alloys, which displayed finer microstructural features with pronounced phase contrast. In

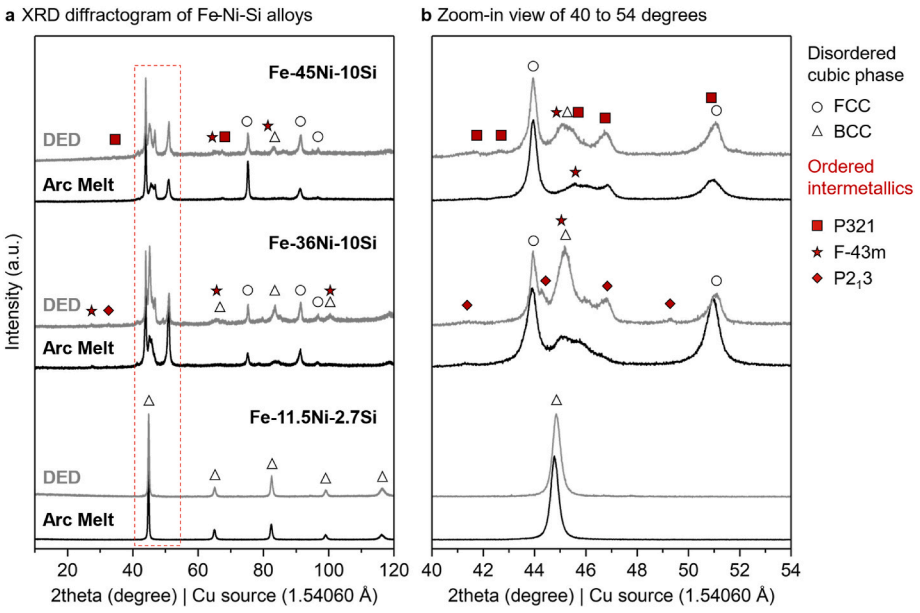

Fig. 4. Comparison of the XRD patterns of DED and arc melted Fe–Ni–Si alloys. (a) Full diffractograms (10°–120°) show substantially higher fractions of ordered intermetallic phases in high-Ni–Si DED alloys compared to the arc melted counterparts. (b) Magnified view (40°–54°) highlights additional overlapping peaks associated with ordered Ni–Si intermetallics in the DED samples.

general, DED processing resulted in finer microstructures than arc melting, consistent with the higher cooling rates associated with additive manufacturing. It is noted that these observations are qualitative, as quantitative grain size measurements were not performed.

EBSD inverse pole figure (IPF) maps (Fig. 5c) and corresponding phase maps (Fig. 5d) provide further insight into the crystallographic and phase distributions between the two processing routes. DED-fabricated samples displayed weak texture but showed pronounced intergranular connectivity of the secondary phases, forming continuous networks along grain boundaries. In contrast, the arc melted samples displayed more homogeneous phase distribution and, particularly at higher Ni content, developed textured FCC grains, suggesting an orientation selection during slower solidification.

The spatial distribution of phases revealed by EBSD is critical for understanding the mechanical behaviour. In DED samples, the formation of interconnected intergranular phase networks effectively partitioned the microstructure, limiting the continuity of the ductile matrix. This phase connectivity was significantly reduced in the arc melted samples, where intermetallic phases were more isolated and dispersed.

EDX elemental maps (Fig. 5e–g) confirmed that Ni and Si segregation increased with larger solute content, leading to the formation of Ni–Si-enriched intergranular regions in the high-Ni–Si alloys. This chemical partitioning directly correlates with the phase maps and is consistent with the strong thermodynamic affinity between Ni and Si discussed in Section 3.1 (Fig. 2). The segregation-driven formation of intergranular intermetallic networks therefore represents a key microstructural feature governing mechanical response.

Nanoindentation mapping (Fig. 6) provides direct evidence of the local mechanical consequences of this microstructural architecture. Hardness peaks of ~12 GPa were observed at intergranular regions enriched in Ni and Si, corresponding to intermetallic phases. In contrast, the Fe-rich grain interiors exhibited significantly lower hardness values of ~5 GPa. This strong spatial heterogeneity confirmed that the intermetallic phases dominate the strengthening response.

Importantly, the interconnected nature of these hard intergranular phases not only enhanced hardness but also promoted strain localization and reduced the capacity for plastic deformation. This explains the coexistence of high hardness and brittle behaviour observed in DED-fabricated high-Ni–Si alloys. In contrast, the more homogeneous phase distribution in arc melted samples resulted in a more uniform mechanical response and improved resistance to cracking.

These observations established a direct processing–structure–property relationship. DED promoted non-equilibrium segregation and the formation of interconnected intergranular intermetallic networks, leading to high hardness but also embrittlement and cracking. In contrast, arc melting suppressed intergranular phase connectivity through enhanced homogenization, resulting in coarser but more mechanically stable microstructures. This comparison highlights the critical role of phase architecture, particularly intermetallic connectivity, in governing the mechanical performance of Fe–Ni–Si alloys.

3.5. *Mechanical, magnetic, and electrical performance of Fe–Ni–Si alloys*

Table 3 and Fig. 7 summarizes the mechanical, electrical and magnetic properties of the three Fe–Ni–Si compositions investigated in this work, benchmarked against reference Fe–Si and Fe–Ni–Co alloys from our prior work [17,18]. The results reveal a clear trade-off between intermetallic phase fraction and multifunctional performance.

Vickers hardness. The Vickers hardness of DED-fabricated samples was consistently higher than those of arc melted counterparts, particularly for Fe–36Ni–10Si and Fe–45Ni–10Si. These alloys exhibited hardness values of ~576 HV and ~562 HV, respectively, approaching the upper range reported for Fe-based soft magnetic materials. The higher hardness in DED samples is primarily attributed to the increased mass fraction and the connectivity of ordered intermetallic phases, as established in Sections 3.1–3.4. In contrast, Fe–11.5Ni–2.7Si showed comparable hardness for both processing routes, consistent with its single-phase BCC structure. Although DED samples exhibited finer microstructural features, the dominant strengthening mechanism arises from intermetallic phase content and distribution rather than grain size alone. The slightly lower hardness compared to compositionally graded samples (>600 HV) reflects the absence of localized peak compositions in single-composition samples.

Mechanical properties. As discussed earlier, DED-fabricated samples were not suitable for tensile testing due to extensive cracking and brittle behaviour, and tensile properties were therefore reported only for arc melted alloys. Representative engineering stress–strain curves are provided in Fig. 7a. Arc melted Fe–11.5Ni–2.7Si exhibited a yield

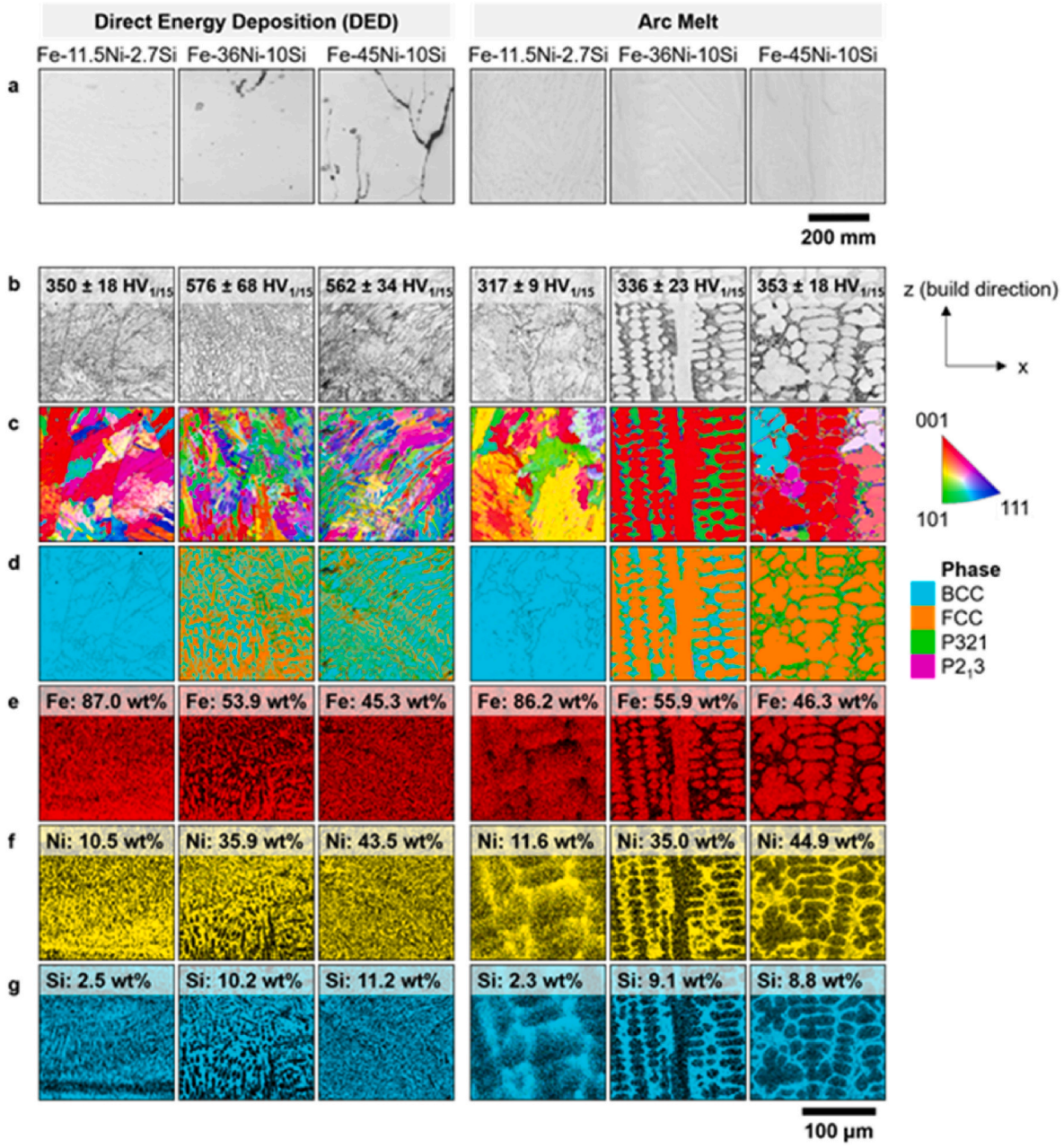

Fig. 5. Microstructural comparison of Fe–Ni–Si alloys fabricated by DED and arc melting. (a) Optical micrographs show cracks in DED high-Ni–Si alloys, cracks are absent in DED Fe–11.5Ni–2.7Si and all arc melted samples. (b–d) EBSD maps demonstrate finer grains and higher intergranular connectivity in DED samples, versus textured FCC grains in arc melted samples. (e–g) EDX maps confirm the greater extent of Ni–Si segregation with increasing solute content, and intermetallic network formation along grain boundaries.

strength (YS) of 551 MPa, an ultimate tensile strength (UTS) of 709 MPa, and an elongation to failure of 4.8%. This performance exceeded that of Fe–4.3Si (2.3% elongation) and Fe–15.2Si (0.4% elongation) while maintaining higher strength (Fig. 7a). It also surpassed the elongation for the high-cost Fe–20Ni–20Co alloy (~1.6%), although the latter achieved higher UTS (~1167 MPa).

The improved mechanical performance of Fe–11.5Ni–2.7Si was attributed to its single-phase BCC matrix and the absence of interconnected intergranular intermetallic networks, enabling more uniform plastic deformation. In contrast, arc melted Fe–36Ni–10Si and Fe–45Ni–10Si exhibited higher strength (YS ~413–535 MPa; UTS ~677–696 MPa) but significantly reduced ductility due to the presence of intermetallic phases. Increasing Ni content increased strength but further reduced ductility, reflecting the increasing fraction of brittle ordered phases.

Magnetic properties. Both DED and arc melted Fe–11.5Ni–2.7Si exhibited a saturation magnetization of 199–204 emu/g and coercivity between 14.6 and 22.5 Oe. These values are comparable to Fe–4.3Si (~200 emu/g, ~10 Oe) and superior to Fe–15.2Si (~95 emu/g, ~10 Oe), despite the presence of alloying elements that typically reduce magnetic moment.

This behaviour indicates that the solid-solution BCC matrix maintains ferromagnetic exchange pathways while limiting domain wall pinning associated with the secondary phases and residual stresses. In contrast, Fe–36Ni–10Si and Fe–45Ni–10Si exhibited substantially lower saturation magnetization (35–47 emu/g) and higher coercivity (~88–174 Oe), consistent with their high intermetallic content and intergranular phase networks. The relatively low coercivity observed in

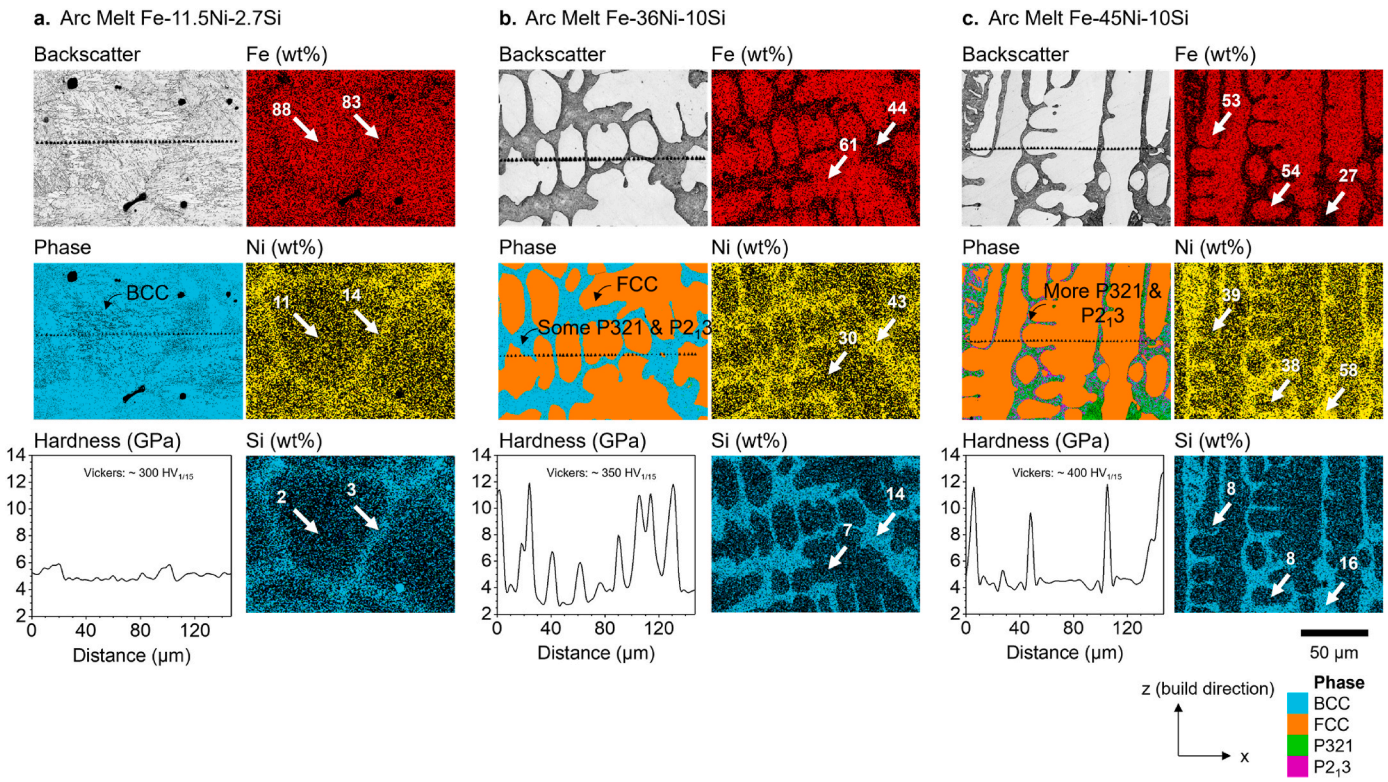

Fig. 6. Nanoindentation mapping of arc melted Fe–Ni–Si alloys. Hardness peaks of ~12 GPa are observed at Ni–Si-rich intergranular regions, while Fe-rich grains show lower hardness (~5 GPa). The results confirm that the intermetallic content is the primary source of high hardening. (a) Fe–11.5Ni–2.7Si, (b) Fe–36Ni–10Si, (c) Fe–45Ni–10Si.

Table 3
Mechanical, electrical, and magnetic properties of Fe–Ni–Si alloys fabricated by DED and arc melting, benchmarked against Fe–Si and Fe–Ni–Co alloys.

Process/Nominal Composition	Vickers Hardness ($HV_{1/15}$)	Young's Modulus (GPa)	Yield Strength (MPa)	Ultimate Tensile Strength (MPa)	Elongation (%)	Resistivity (μΩ cm)	Saturation Magnetization (emu/g)	Coercivity (Oe)	Ref.
This work									
DED Fe–45Ni–10Si	562 ± 34	Brittle	Brittle	Brittle	Brittle	340	47	88.2	This work
DED Fe–36Ni–10Si	576 ± 68	Brittle	Brittle	Brittle	Brittle	178	43	138.9	This work
DED Fe–11.5Ni–2.7Si	350 ± 18	Brittle	Brittle	Brittle	Brittle	122	204	22.5	This work
Arc Melt Fe–45Ni–10Si	353 ± 18	134 ± 3	535 ± 20	696 ± 29	1.3 ± 0.1	349	46	10.5	This work
Arc Melt Fe–36Ni–10Si	336 ± 23	132 ± 2	413 ± 13	677 ± 19	1.7 ± 0.1	174	35	174.1	This work
Arc Melt Fe–11.5Ni–2.7Si	**317 ± 9**	**155 ± 6**	**551 ± 42**	**709 ± 24**	**4.8 ± 0.2**	**105**	**199**	**14.6**	This work
Prior work									
DED Fe–15.2Si	600 – 700	258 ± 76	71 ± 17	91 ± 5	0.4	100 – 120	~95	~10	[18]
DED Fe–4.3Si	200 – 300	347 ± 52	545 ± 48	548 ± 16	2.3	60 – 80	~200	~10	[18]
DED Fe–Ni Graded	~100	-	-	-	-	25 – 70	100 – 150	0.5 – 2	[17]
DED Fe–40Ni–20Co	~150	223.18	298	465	60.1	16	147	8	[17]
DED Fe–20Ni–20Co	~330	244.31	1001	1167	1.57	32	206	12	[17]

"Brittle" indicates catastrophic fracture during specimen preparation or testing, precluding reliable tensile measurements. Values reported as ranges reflect variability across composition or processing windows in the cited studies.

arc melted Fe–45Ni–10Si (10.5 Oe) further underscores the sensitivity of magnetic response to phase distribution and microstructural homogeneity. Saturation magnetization is an intrinsic material property and is generally insensitive to the microstructure. Coercivity, on the other hand, is affected by the composition, microstructure and phases present.

Electrical resistivity. Fe–11.5Ni–2.7Si exhibited an electrical resistivity of 105 μΩ cm, an order of magnitude higher than pure Fe (~10 μΩ cm) and Fe–Ni–Co soft magnetic alloys (~30–50 μΩ cm) [17,52]. Elevated resistivity is critical for minimizing eddy current losses in high-frequency applications. The ability of Fe–11.5Ni–2.7Si to simultaneously achieve high resistivity, good mechanical performance, and magnetic softness therefore represents a significant departure from conventional property trade-offs (Fig. 7b). The high-Ni–Si alloys exhibited even higher electrical resistivity (~340 μΩ cm for Fe–45Ni–10Si and ~170 μΩ cm for Fe–36Ni–10Si), but at the expense of ductility and magnetic performance. The electrical resistivity values are

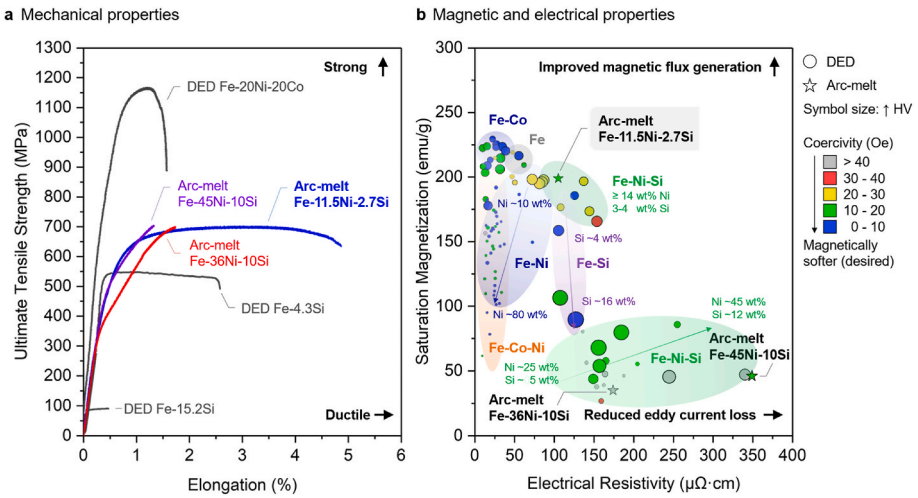

Fig. 7. Benchmarking properties of Fe–Ni–Si alloys. (a) Tensile results highlight superior strength–ductility synergy of Fe–11.5Ni–2.7Si compared to Fe–Si and Fe–Ni–Co. (b) Resistivity versus saturation magnetization plot shows Fe–11.5Ni–2.7Si achieves an attractive property balance: high resistivity (105 μΩ cm) alongside magnetic properties (~199 emu/g, 14 Oe).

similar between the samples processed with the different methods, indicating that the microstructural effects are not significant here.

Comparison with cobalt-containing alloys. Benchmarking against Fe–20Ni–20Co, a widely used soft magnetic alloy with high strength (~1167 MPa) but low resistivity (~32 μΩ cm) and poor elongation (~1.6%) values [17], further highlights the unique position of Fe–11.5Ni–2.7Si. While Co-containing alloys offer superior tensile strength, they are constrained by cost, resource criticality, and limited resistivity. In contrast, the Fe–Ni–Si alloy presented here is free from critical elements, exhibits a balanced combination of mechanical, magnetic, and electrical properties, and can be produced using scalable, low-cost melting techniques. These results establish the potential of Fe–11.5Ni–2.7Si as a promising multi-functional magnetic structural alloy, and highlight the critical role of composition and processing route in tailoring coupled mechanical–magnetic–electrical performance.

Comparison with amorphous and nanocrystalline alloys. Taking reference from Fiorillo et al. [53], amorphous alloys are Fe-based $Fe_{78}B_{13}Si_9$ and Co-based $Co_{67}Fe_4B_{14.5}Si_{14.5}$, while nanocrystalline alloys include materials like FINEMET ($Fe_{73.5}Cu_1Nb_3Si_{13.5}B_9$) and NANOPERM ($Fe_{86}Cu_1Zr_7B_6$). These amorphous and nanocrystalline alloys have much lower coercivity values (<0.1 Oe) than the 3 Fe–Ni–Si alloys discussed in this work, and comparable electrical resistivity (118–140 μΩ cm) to Fe–11.5Ni–2.7Si but lower than that of Fe–36Ni–10Si and Fe–45Ni–10Si. The saturation magnetization of amorphous/nanocrystalline alloys is in the range of 61–167 emu/g, higher than Fe–36Ni–10Si and Fe–45Ni–10Si but lower than Fe–11.5Ni–2.7Si.

In terms of mechanical properties, the Vickers hardness values of amorphous and nanocrystalline alloys are ~800 HV, much higher than the 3 alloys. Amorphous alloys also possess higher tension yield stress and fracture stress of 700 MPa and 2800 MPa respectively. Nanocrystalline FINEMET alloys on the other hand have tension yield stress and fracture stress of only 150 MPa each. As mentioned in the Introduction, these amorphous and nanocrystalline have its own challenges in fabrication, and in turn limited commercial adoption.

3.6. *Structure–property correlations across compositions*

The contrasting behaviour of DED and arc melted Fe–Ni–Si alloys highlights the central role of intermetallic phase fraction and its spatial distribution in governing the coupled mechanical, magnetic, and electrical properties (Fig. 8). Across all compositions investigated, higher fractions of ordered intermetallic phases systematically enhanced hardness and electrical resistivity, while reducing ductility and saturation magnetization.

DED-fabricated alloys, particularly Fe–36Ni–10Si and Fe–45Ni–10Si, contained intermetallic phase fractions in the range of ~30–56 vol% (Fig. 8a). These alloys exhibited Vickers hardness values approaching 600 HV (Fig. 8b) but displayed severe brittleness (Fig. 8c and d). This behaviour arose from the formation of interconnected intergranular intermetallic networks, which effectively blocked dislocation motion but also partitioned the microstructure, limiting the continuity of the ductile matrix and promoting strain localization and crack propagation. In contrast, arc melted samples exhibited lower intermetallic fractions (~20–30 vol%) and reduced phase connectivity, resulting in lower hardness (300–350 HV) but improved elongation to failure. This inverse relationship reflects the fundamental trade-off between strengthening through ordered-phase formation and the preservation of plastic deformability, as continuous intergranular intermetallic networks impede dislocation motion but also promote strain localization and premature fracture.

Electrical resistivity increased systematically with larger intermetallic phase fraction (Fig. 8e). The elevated resistivity is attributed to enhanced electron scattering at the matrix–intermetallic interfaces. While this is beneficial for reducing eddy current losses in high frequency applications, it is coupled with the formation of intermetallic phases that degrade ductility and magnetic properties.

Saturation magnetization decreased monotonically with increasing ordered-phase content (Fig. 8f), reflecting progressive dilution of the ferromagnetic Fe-rich matrices by non-magnetic or weakly magnetic intermetallic phases. The saturation magnetization is presented in Tesla (T) here, to account for the differences in alloy density that can influence volumetric magnetization comparisons. The saturation magnetization values range from 0.34T to 0.46T for Fe–36Ni–10Si and Fe–45Ni–10Si, which is quite low compared to common soft magnetic alloys, which is in the range of 1.6T to 2.35T [53]. Fe–11.5Ni–2.7Si however, is attractive, with a comparable saturation magnetization of 1.96T to 2.01T. Coercivity (Fig. 8g) did not exhibit any clear dependence on the intermetallic fraction, suggesting that it is governed by a complex interplay of composition, microstructure, and defect structures.

Taken together, these correlations established that the intermetallic phase fraction and its connectivity act as the key microstructural parameter linking the processing route to multifunctional properties in Fe–Ni–Si alloys. High intermetallic content promoted hardness and resistivity but induces embrittlement and magnetic degradation, whereas the suppression of intermetallic network formation enabled a more

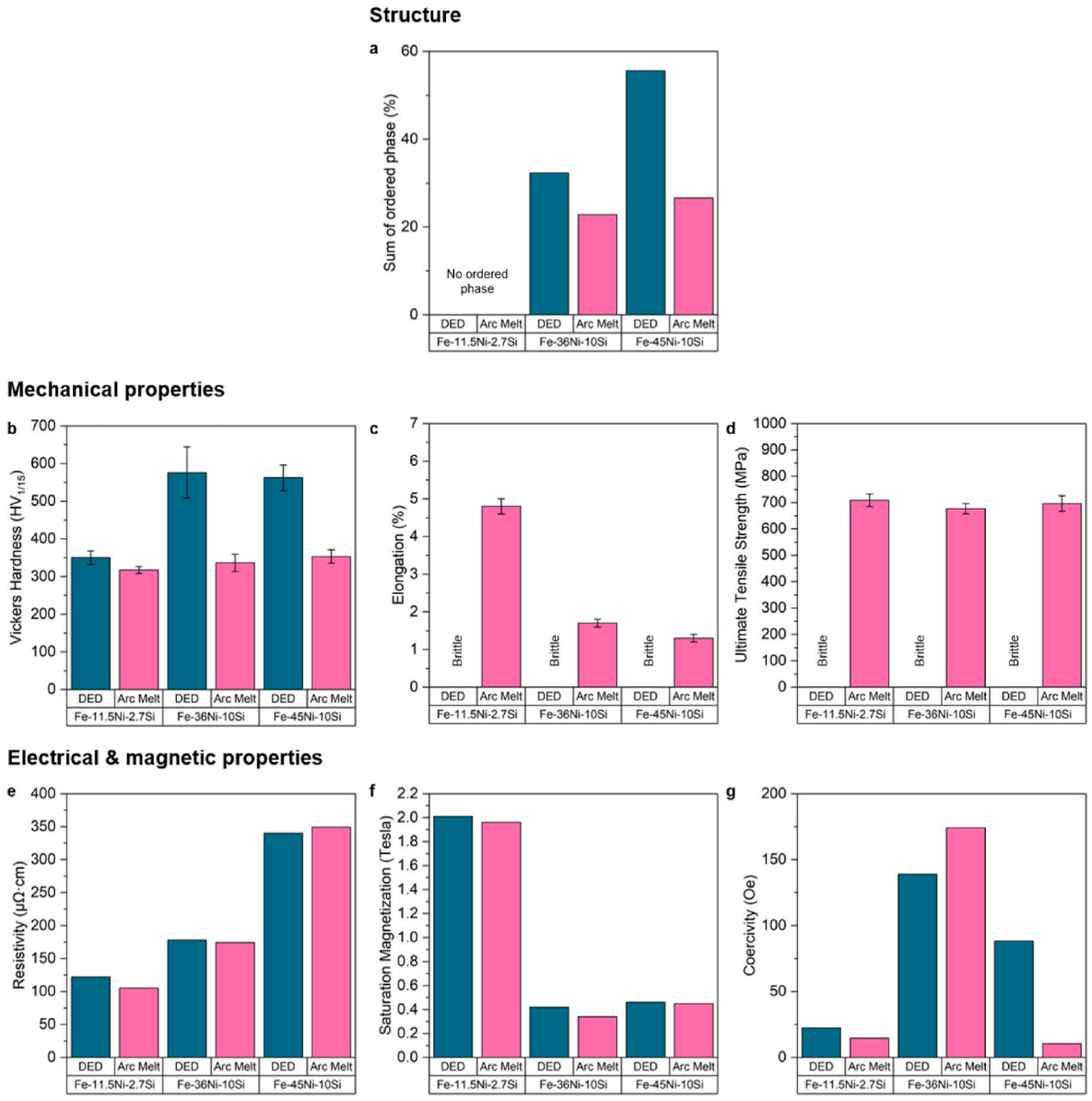

Fig. 8. Structure–property correlations in Fe–Ni–Si alloys fabricated by DED and arc melting. (a) Sum of ordered phases (intermetallic phase fraction), (b) Vickers hardness, (c) elongation, (d) ultimate tensile strength, (e) electrical resistivity, (f) saturation magnetization and (g) coercivity.

balanced property profile.

Specifically, Fe–11.5Ni–2.7Si, stabilized as a single-phase BCC matrix, achieved a favourable combination of strength, ductility, magnetic response, and electrical resistivity. This demonstrates that tailoring the intermetallic phase fraction through both composition and processing provides a viable design strategy for developing multifunctional alloys.

4. Conclusions

Fe–Ni–Si alloys fabricated by DED and arc melting exhibited two distinct composition–processing regimes governed by solidification kinetics and intermetallic phase formation. High-Ni, high-Si alloys undergo pronounced non-equilibrium segregation during DED, leading to the formation of interconnected intergranular intermetallic network formation that resulted in high hardness but also severe cracking and embrittlement. In contrast, the lower solute Fe–11.5Ni–2.7Si composition stabilized as a single-phase BCC matrix under both processing routes.

The arc melted Fe–11.5Ni–2.7Si composition demonstrated a favourable combination of mechanical and functional properties, including yield strength (551 MPa), ultimate tensile strength (709 MPa), ductility (4.8%), saturation magnetization (~199 emu/g), coercivity (~14 Oe), and high electrical resistivity (105 μΩ cm). This balanced property set is achieved without the use of critical alloying elements such as cobalt and under conventional bulk processing conditions.

A unified structure–property relationship has been established, in which both the fraction and connectivity of ordered intermetallic phases govern the trade-off between hardness, ductility, magnetic properties and electrical resistivity. Increasing the intermetallic phase content enhanced hardness and electrical resistivity through interfacial strengthening and electron scattering, but simultaneously reduced ductility and magnetic response due to strain localization and dilution of the ferromagnetic matrix. These findings demonstrate that controlling intermetallic phase fraction and morphology through composition and processing provides a viable design strategy for developing multifunctional magnetic structural alloys. In particular, Fe–11.5Ni–2.7Si emerged as a promising candidate for applications requiring a combination of mechanical integrity, magnetic properties and reduced eddy

current losses. Future work can also investigate the effects of heat treatment on microstructure to further optimize mechanical and magnetic properties. Saturation magnetostriction coefficient, which was not measured in this work, is important for rotating machine applications to minimize operating noise, and its measurements will also be considered for material optimization.

Declaration of competing interest

The authors declare that they have no known competing financial interests or personal relationships that could have appeared to influence the work reported in this paper.

Acknowledgements

This work was supported by the Agency for Science, Technology and Research (A*STAR), Singapore, through the AME Programmatic Fund under Grant Nos. A1898b0043 and A18B1b0061, and by the National Research Foundation, Singapore (Award ID NRF-CRP29-2022-0002) under its 29th Competitive Research Programme. The authors also acknowledge financial support from the Åforsk Foundation, Sweden (Award ID 24-571), and from the Areas of Advance in Production, Materials, and Energy at Chalmers University of Technology.

Data availability

Data will be made available on request.

References

[1] Sarkar SK, Keskar N, Tan LP, Ingale T, Chesetti A, Dasari S, Davidson KP, Chaudhary V, Dahotre N, Ramanujan RV, Banerjee R. A magnetically soft yet mechanically strong and ductile Ta free CoFeNi high entropy alloy with Al and Ti additions. Nat Commun 2026;17(1):2890. https://doi.org/10.1038/s41467-026-68891-6.

[2] Cullity BD, Graham CD. Soft magnetic materials, introduction to magnetic materials. 2008. p. 439–76. https://doi.org/10.1002/9780470386323.ch13.

[3] Silveyra JM, Ferrara E, Huber DL, Monson TC. Soft magnetic materials for a sustainable and electrified world. Science 2018;362(6413). https://doi.org/10.1126/science.aao0195. eaao0195.

[4] Refaie AE-. Toward a sustainable more electrified future: the role of electrical machines and drives. IEEE Electrif Mag 2019;7(1):49–59. https://doi.org/10.1109/MELE.2018.2889551.

[5] Barefield EK, Busch DH, Nelson SM. Iron, cobalt, and nickel complexes having anomalous magnetic moments. Q Rev Chem Soc 1968;22(4):457–98. https://doi.org/10.1039/QR9682200457.

[6] Pfeifer F, Radeloff C. Soft magnetic Ni-Fe and Co-Fe alloys - some physical and metallurgical aspects. J Magn Magn Mater 1980;19(1):190–207. https://doi.org/10.1016/0304-8853(80)90592-2.

[7] Sundar RS, Deevi SC. Soft magnetic FeCo alloys: alloy development, processing, and properties. Int Mater Rev 2005;50(3):157–92. https://doi.org/10.1179/174328005X14339.

[8] McHenry ME, Ohodnicki PR, Moon S-R, Krimer Y. Soft magnetic materials. In: Franco V, Dodrill B, editors. Magnetic measurement techniques for materials characterization. Cham: Springer International Publishing; 2021. p. 665–82. https://doi.org/10.1007/978-3-030-70443-8_21.

[9] Roberts S, Gunn G. In: Cobalt, critical metals handbook; 2014. p. 122–49. https://doi.org/10.1002/9781118755341.ch6.

[10] Ryu H-H, Sun HH, Myung S-T, Yoon CS, Sun Y-K. Reducing cobalt from lithium-ion batteries for the electric vehicle era. Energy Environ Sci 2021;14(2):844–52. https://doi.org/10.1039/D0EE03581E.

[11] Zeng A, Chen W, Rasmussen KD, Zhu X, Lundhaug M, Müller DB, Tan J, Keiding JK, Liu L, Dai T, Wang A, Liu G. Battery technology and recycling alone will not save the electric mobility transition from future cobalt shortages. Nat Commun 2022;13(1):1341. https://doi.org/10.1038/s41467-022-29022-z.

[12] von Goldbeck OK. Fe—Si Iron—Silicon. In: von Goldbeck OK, editor. IRON—Binary phase diagrams. Berlin, Heidelberg: Springer Berlin Heidelberg; 1982. p. 136–9. https://doi.org/10.1007/978-3-662-08024-5_62.

[13] Haiji H, Okada K, Hiratani T, Abe M, Ninomiya M. Magnetic properties and workability of 6.5% Si steel sheet. J Magn Magn Mater 1996;160:109–14. https://doi.org/10.1016/0304-8853(96)00128-X.

[14] Shin JS, Bae JS, Kim HJ, Lee HM, Lee TD, Lavernia EJ, Lee ZH. Ordering–disordering phenomena and micro-hardness characteristics of B2 phase in Fe–(5–6.5%)Si alloys. Mater Sci Eng, A 2005;407(1):282–90. https://doi.org/10.1016/j.msea.2005.07.012.

[15] Cui S, Jung I-H. Critical reassessment of the Fe-Si system. Calphad 2017;56:108–25. https://doi.org/10.1016/j.calphad.2016.11.003.

[16] Ouyang G, Chen X, Liang Y, Macziewski C, Cui J. Review of Fe-6.5 wt%Si high silicon steel—A promising soft magnetic material for sub-kHz application. J Magn Magn Mater 2019;481:234–50. https://doi.org/10.1016/j.jmmm.2019.02.089.

[17] Teh WH, Chaudhary V, Chen S, Lim SH, Wei F, Lee JY, Wang P, Padhy SP, Tan CC, Ramanujan RV. High throughput multi-property evaluation of additively manufactured Co-Fe-Ni materials libraries. Addit Manuf 2022;58:102983. https://doi.org/10.1016/j.addma.2022.102983.

[18] Teh WH, Tan LP, Chen S, Wei F, Lee JJ, Padhy SP, Chaudhary V, Tan CC, Ramanujan RV. Breaking conventional limits of silicon content in Fe-xSi magnetic alloys through additive manufacturing. J Alloys Compd 2024;983:173829. https://doi.org/10.1016/j.jallcom.2024.173829.

[19] Teh WH, Tan LP, Chen S, Lee JJ, Wei F, Padhy SP, Chaudhary V, Tan CC, Ramanujan RV. Multi-property materials discovery from additively manufactured compositionally graded fe-ni-si alloys. Acta Mater 2026;302:121625. https://doi.org/10.1016/j.actamat.2025.121625.

[20] Herzer G. Modern soft magnets: amorphous and nanocrystalline materials. Acta Mater 2013;61(3):718–34. https://doi.org/10.1016/j.actamat.2012.10.040.

[21] Liu T, Li F, Wang A, Xie L, He Q, Luan J, He A, Wang X, Liu CT, Yang Y. High performance Fe-based nanocrystalline alloys with excellent thermal stability. J Alloys Compd 2019;776:606–13. https://doi.org/10.1016/j.jallcom.2018.10.319.

[22] Liu D, Liu X, Wang J, Mao X, Xu X, Fan XA. The influence of Fe nanoparticles on microstructure and magnetic properties of Fe-6.5wt%Si soft magnetic composites. J Alloys Compd 2020;835:155215. https://doi.org/10.1016/j.jallcom.2020.155215.

[23] Shi X, Chen X, Wan K, Zhang B, Duan P, Zhang H, Zeng X, Liu W, Su H, Zou Z, Du Y. Enhanced magnetic and mechanical properties of gas atomized Fe-Si-Al soft magnetic composites through adhesive insulation. J Magn Magn Mater 2021;534:168040. https://doi.org/10.1016/j.jmmm.2021.168040.

[24] Najgebauer M. Advances in contemporary soft magnetic materials – a review. 2023 10th international conference on electrical, electronic and computing engineering (IcETRAN). 2023. p. 1–10. https://doi.org/10.1109/IcETRAN59631.2023.10192209.

[25] Han L, Maccari F, Souza Filho IR, Peter NJ, Wei Y, Gault B, Gutfleisch O, Li Z, Raabe D. A mechanically strong and ductile soft magnet with extremely low coercivity. Nature 2022;608(7922):310–6. https://doi.org/10.1038/s41586-022-04935-3.

[26] Ma Y, Kou Z, Yang W, He A, Dong Y, Man Q, Liu H, Li Z, Inoue A, Li J. A one-step fabrication of soft-magnetic high entropy alloy fiber with excellent strength and flexibility. Nat Commun 2024;15(1):10549. https://doi.org/10.1038/s41467-024-54984-7.

[27] Dai M, Zhang Y, Li X, Schönecker S, Han L, Xie R, Shen C, Zhang H. Data-driven design of mechanically hard soft magnetic high-entropy alloys. Adv Sci 2025;12(19):2500867. https://doi.org/10.1002/advs.202500867.

[28] Oikawa K, Wulff L, Iijima T, Gejima F, Ohmori T, Fujita A, Fukamichi K, Kainuma R, Ishida K. Promising ferromagnetic Ni–Co–Al shape memory alloy system. Appl Phys Lett 2001;79(20):3290–2. https://doi.org/10.1063/1.1418259.

[29] Nguyen VQ, Ahmed AS, Ramanujan RV. Morphing soft magnetic composites. Adv Mater 2012;24(30):4041–54. https://doi.org/10.1002/adma.201104994.

[30] Donnelly C, Hierro-Rodríguez A, Abert C, Witte K, Skoric L, Sanz-Hernández D, Finizio S, Meng F, McVitie S, Raabe J, Suess D, Cowburn R, Fernández-Pacheco A. Complex free-space magnetic field textures induced by three-dimensional magnetic nanostructures. Nat Nanotechnol 2022;17(2):136–42. https://doi.org/10.1038/s41565-021-01027-7.

[31] Wang W, Fan J, Li C, Yu Y, Wang A, Li S, Liu J. Low-loss soft magnetic materials and their application in power conversion: progress and perspective. Energies 2025:482. https://doi.org/10.3390/en18030482.

[32] Theisen EA. Recent advances and remaining challenges in manufacturing of amorphous and nanocrystalline alloys. IEEE Trans Magn 2022;58(8):1–7. https://doi.org/10.1109/TMAG.2022.3163713.

[33] Yang X, Cui X, Jin G, Liu J, Chen Y, Liu Z. Soft magnetic property of (Fe60Co35Ni5)78 Si6B12Cu1Mo3 alloys by laser additive manufacturing. J Magn Magn Mater 2018;466:75–80. https://doi.org/10.1016/j.jmmm.2018.06.085.

[34] Chaudhary V, Mantri SA, Ramanujan RV, Banerjee R. Additive manufacturing of magnetic materials. Prog Mater Sci 2020;114:100688. https://doi.org/10.1016/j.pmatsci.2020.100688.

[35] Lamichhane TN, Sethuraman L, Dalagan A, Wang H, Keller J, Paranthaman MP. Additive manufacturing of soft magnets for electrical machines—a review. Mater Today Phys 2020;15:100255. https://doi.org/10.1016/j.mtphys.2020.100255.

[36] Nartu MSKKY, Jagetia A, Chaudhary V, Mantri SA, Ivanov E, Dahotre NB, Ramanujan RV, Banerjee R. Magnetic and mechanical properties of an additively manufactured equiatomic CoFeNi complex concentrated alloy. Scr Mater 2020;187:30–6. https://doi.org/10.1016/j.scriptamat.2020.05.063.

[37] Selema A, Beretta M, Van Coppenolle M, Tiismus H, Kallaste A, Ibrahim MN, Rombouts M, Vleugels J, Kestens LAI, Sergeant P. Evaluation of 3D-Printed magnetic materials for additively-manufactured electrical machines. J Magn Magn Mater 2023;569:170426. https://doi.org/10.1016/j.jmmm.2023.170426.

[38] Kustas AB, Fancher CM, Whetten SR, Dagel DJ, Michael JR, Susan DF. Controlling the extent of atomic ordering in intermetallic alloys through additive manufacturing. Addit Manuf 2019;28:772–80. https://doi.org/10.1016/j.addma.2019.06.020.

[39] Babuska TF, Wilson MA, Johnson KL, Whetten SR, Curry JF, Rodelas JM, Atkinson C, Lu P, Chandross M, Krick BA, Michael JR, Argibay N, Susan DF, Kustas AB. Achieving high strength and ductility in traditionally brittle soft magnetic intermetallics via additive manufacturing. Acta Mater 2019;180:149–57. https://doi.org/10.1016/j.actamat.2019.08.044.

[40] Haines MP, List F, Carver K, Leonard DN, Plotkowski A, Fancher CM, Dehoff RR, Babu SS. Role of scan strategies and heat treatment on grain structure evolution in Fe-Si soft magnetic alloys made by laser-powder bed fusion. Addit Manuf 2022;50:102578. https://doi.org/10.1016/j.addma.2021.102578.

[41] Shen X, Meng F, Lau KB, Wang P, Lee CHT. Texture and microstructure characterizations of Fe-3.5wt%Si soft magnetic alloy fabricated via laser powder bed fusion. Mater Charact 2022;189:112012. https://doi.org/10.1016/j.matchar.2022.112012.

[42] Goodall AD, Yiannakou G, Chechik L, Mitchell RL, Jewell GW, Todd I. Geometrical control of eddy currents in additively manufactured Fe-Si. Mater Des 2023;230:112002. https://doi.org/10.1016/j.matdes.2023.112002.

[43] Tokunaga T, Nishio K, Ohtani H, Hasebe M. Thermodynamic assessment of the Ni–Si system by incorporating *ab initio* energetic calculations into the CALPHAD approach. Calphad 2003;27(2):161–8. https://doi.org/10.1016/S0364-5916(03)00049-X.

[44] Cacciamani G, Dinsdale A, Palumbo M, Pasturel A. The Fe–Ni system: thermodynamic modelling assisted by atomistic calculations. Intermetallics 2010;18(6):1148–62. https://doi.org/10.1016/j.intermet.2010.02.026.

[45] Vyatskikh AL, Wang X, Haley J, Zheng B, Valdevit L, Lavernia EJ, Schoenung JM. Residual stress mitigation in directed energy deposition. Mater Sci Eng, A 2023;871:144845. https://doi.org/10.1016/j.msea.2023.144845.

[46] Li C, Liu ZY, Fang XY, Guo YB. Residual stress in metal additive manufacturing. Proced CIRP 2018;71:348–53. https://doi.org/10.1016/j.procir.2018.05.039.

[47] Farshidianfar MH, Khajepour A, Gerlich AP. Effect of real-time cooling rate on microstructure in laser additive manufacturing. J Mater Process Technol 2016;231:468–78. https://doi.org/10.1016/j.jmatprotec.2016.01.017.

[48] Huang Y, Ansari M, Asgari H, Farshidianfar MH, Sarker D, Khamesee MB, Toyserkani E. Rapid prediction of real-time thermal characteristics, solidification parameters and microstructure in laser directed energy deposition (powder-fed additive manufacturing). J Mater Process Technol 2019;274:116286. https://doi.org/10.1016/j.jmatprotec.2019.116286.

[49] Munitz A, Bamberger AM, Wannaparhun S, Abbaschian R. Effects of supercooling and cooling rate on the microstructure of Cu–Co–Fe alloys. J Mater Sci 2006;41(10):2749–59. https://doi.org/10.1007/s10853-006-5598-8.

[50] Pfeifer H. Industrial furnaces - status and research challenges. Energy Proc 2017;120:28–40. https://doi.org/10.1016/j.egypro.2017.07.153.

[51] Preuß B, Lindner T, Uhlig T, Wagner G, Lampke T. Niobium and molybdenum as alloying constituents in Al0.3CoCrFeNi to develop eutectic high-entropy alloys for HVOF spraying. J Therm Spray Technol 2023;32(2):415–24. https://doi.org/10.1007/s11666-022-01417-w.

[52] Metals E. Kovar® Typical Properties & Standards – ASTM F15. https://www.efinemetals.com/controlled-expansion-alloys/kovar-astm-f-15-pernifer-nilo-rod-bar-sheet-plate/kovar-properties/. [Accessed 1 October 2025].

[53] Fiorillo F, Bertotti G, Appino C, Pasquale M. Soft magnetic materials. Wiley Encyclopedia of Electrical and Electronics Engineering 2016:1–42. https://doi.org/10.1002/047134608X.W4504.pub2.